

FIDUCIAL STELLAR POPULATION SEQUENCES FOR THE $u'g'r'i'z'$ SYSTEM¹

James L. Clem² and Don A. Vandenberg

*Department of Physics & Astronomy, University of Victoria, P.O. Box 3055, Victoria,
B.C. V8W 3P6, Canada*

`jclem@uvastro.phys.uvic.ca, vandenbe@uvic.ca`

and

Peter B. Stetson

*Dominion Astrophysical Observatory, Herzberg Institute of Astrophysics, National Research
Council, 5071 West Saanich Road, Victoria, BC V9E 2E7, Canada*

`Peter.Stetson@nrc.gc.ca`

ABSTRACT

We describe an extensive observational project that has obtained high-quality and homogeneous photometry for a number of different Galactic star clusters (including M92, M13, M3, M71, and NGC 6791) spanning a wide range in metallicity ($-2.3 \lesssim [\text{Fe}/\text{H}] \lesssim +0.4$), as observed in the $u'g'r'i'z'$ passbands with the MegaCam wide-field imager on the Canada-France-Hawaii Telescope. By employing these purest of stellar populations, fiducial sequences have been defined from color-magnitude diagrams that extend from the tip of the red-giant branch down to approximately 4 magnitudes below the turnoff: these sequences have been accurately calibrated to the standard $u'g'r'i'z'$ system via a set of secondary

¹Based on observations obtained with MegaPrime/MegaCam, a joint project of CFHT and CEA/DAPNIA, at the Canada-France-Hawaii Telescope (CFHT) which is operated by the National Research Council (NRC) of Canada, the Institut National des Science de l'Univers of the Centre National de la Recherche Scientifique (CNRS) of France, and the University of Hawaii.

²Current address: Department of Physics & Astronomy, Louisiana State University, 202 Nicholson Hall, Baton Rouge, LA 70803 USA; `jclem@phys.lsu.edu`

photometric standards located within these same clusters. Consequently, they can serve as a valuable set of empirical fiducials for the interpretation of stellar populations data in the $u'g'r'i'z'$ system.

Subject headings: Hertzsprung-Russell diagram — globular clusters: general — globular clusters: individual (M 92, M 13, M 3, M 71) — open clusters and associations: individual (NGC 6791)

1. Introduction

Recently, the Sloan Digital Sky Survey (SDSS) officially ended its planned five years of sky scanning operations to obtain an unprecedented amount of imaging and spectroscopic data for approximately one-quarter of the sky. The SDSS was carried out on a dedicated 2.5 m telescope equipped with a large-format mosaic CCD to image the entire northern Galactic cap (i.e., $b > 30^\circ$) in five photometric bands and two digital spectrographs to provide spectra for ~ 1 million stars, galaxies, and quasars scattered throughout the imaging area. Although designed to primarily investigate the large-scale structure of the universe, the imaging component of the SDSS has obtained high-quality multicolor photometry for about 10^8 stellar objects in the Milky Way, which represents the largest and most homogeneous database on Galactic stellar populations ever obtained. A notable feature of this database is that it was compiled in a new photometric system consisting of five unique passbands (u' , g' , r' , i' , and z') that were specifically designed for the SDSS to provide continuous coverage over the *entire* optical wavelength range (Fukugita et al. 1996).

While the SDSS was the first to implement the standard $u'g'r'i'z'$ photometric system, analogous versions of these same filters are also currently in use with CCD imagers installed on the Gemini Telescopes, the Canada-France-Hawaii Telescope, and the Hubble Space Telescope. In addition, the very fact that the SDSS has already provided such a large database of photometry of stars and galaxies implies that this photometric system is also becoming widely accepted as the filter set of choice for many planned ground-based observational projects and large-scale sky surveys (e.g., LSST, OmegaCam, Pan-STARRS, VST). Despite this, much of our current observational and theoretical knowledge of resolved stellar populations is based largely on the conventional Johnson-Kron-Cousins $UBV(RI)_C$ photometric system, with a few other studies relying on niche systems like the Strömgen, DDO, Vilnius, and Geneva systems. Consequently, the empirical and theoretical tools that would tie the standard $u'g'r'i'z'$ system to the fundamental properties of observed stellar populations have yet to be defined. Specifically, neither well-calibrated fiducial stellar population sequences nor reliable color- T_{eff} relations are currently available, and yet, without them, it is impos-

sible to fully exploit the capabilities of the SDSS data set as well as complementary studies employing these same filters.

In order to remedy these deficiencies, there is good reason to rely on $u'g'r'i'z'$ observations of star clusters within our own Galaxy. Clusters are the ideal stellar population templates because, despite a handful of exceptions (e.g., ω Cen and M 22), their constituents are believed to be effectively coeval, equi-distant, and nearly identical in terms of their heavy elemental abundances. As a result, their color-magnitude diagrams (CMDs) generally exhibit extremely tight and well-populated sequences of stars that span several orders of magnitude in brightness. Their wide distribution in metallicity is also suitable for characterizing how the photometric properties of stellar populations vary as a function of $[\text{Fe}/\text{H}]$. Consequently, cluster observations offer the perfect data sets to define fiducial stellar population sequences that cover a broad range of stellar parameter space. These sequences serve as a set of empirical “isochrones” that not only facilitate the analysis of other stellar populations data, but also provide calibrators for stellar evolutionary models that are transformed to the observed CMDs via theoretically-derived color- T_{eff} relations (e.g., see Brown et al. 2005). Given the fact that the standard $u'g'r'i'z'$ system was introduced only a short time ago, however, the photometric database for star clusters remains too small to accomplish the tasks mentioned above.

Unfortunately, the SDSS alone cannot provide a sufficient database since (1) the main Sloan survey with the 2.5 m telescope is based on instrumental $ugriz$ passbands that are very similar to, but not quite identical to, the $u'g'r'i'z'$ passbands with which the *standard* Sloan photometric system was defined on the 1.0 m telescope of the USNO Flagstaff Station (Smith et al. 2002).¹ In addition, (2) the brightest stars lying on the red-giant branches (RGBs) of the nearest clusters saturate during ~ 60 s drift-scan exposure times, (3) the SDSS imaging data do not extend deep enough to provide good photometric precision for some of the fainter stars lying on the main sequences in the more distant metal-poor globular clusters, (4) the survey footprint does not reach down to the Galactic plane where the majority of metal-rich open clusters reside. These reasons imply that the SDSS may not be the most ideal source of star cluster photometry for the derivation of fiducial stellar population sequences.

Hence, we recently began an extensive observational project aimed at thoroughly ex-

¹Tucker et al. (2006) have published simple linear transformation equations that relate the instrumental $ugriz$ magnitudes to standard $u'g'r'i'z'$ with reasonable precision (2–3%). At some time in the future more sophisticated transformations may be derived that will enable users to predict standard-system indices from the main-survey observations with a high level of accuracy, at least for normal stellar spectral-energy distributions. Our own instrumental observations from the CFHT have been similarly transformed to the standard $u'g'r'i'z'$ system rather than to the $ugriz$ main-survey system; see below, and Clem et al. (2007).

ploring the nature of stellar populations in the $u'g'r'i'z'$ photometric system via observations of Galactic star clusters. Our first paper (Clem et al. 2007, hereafter Paper I) presented a network of fainter secondary standard stars for the $u'g'r'i'z'$ system in selected star cluster fields to better aid observers on large-aperture telescopes in calibrating their photometry. In fact, the current investigation relies on these standards to calibrate a sample of high-quality and homogeneous $u'g'r'i'z'$ photometry obtained on the 3.6 m Canada-France-Hawaii Telescope (CFHT). This photometry is subsequently employed here to derive a set of accurate stellar population fiducial sequences that span a broad range in both magnitude and metallicity. In our third and final paper (Clem et al. 2008, in preparation) we will utilize these fiducials to test a new grid of theoretical color- T_{eff} relations and bolometric corrections for the $u'g'r'i'z'$ system that have been calculated from synthetic spectra.

The following sections present the details related to the observation, reduction, and compilation of the photometry collected at the CFHT that will be used to derive a set of fiducial stellar population sequences for the $u'g'r'i'z'$ system. In Section 2 we describe the observational setup employed at the CFHT to collect the cluster photometry as well as the data reduction procedure, including the important step of calibrating the observed cluster photometry to the standard $u'g'r'i'z'$ system. Section 3 presents the details of the fiducial sequence derivation process. Finally, a short summary of our results, and a discussion of the usefulness of these fiducials for stellar populations research is given in Section 4.

2. The CFHT Star Cluster Survey

To address the need for fiducial sequences in the $u'g'r'i'z'$ system, an observational program aimed at obtaining high-quality photometry for a number of Galactic star clusters was conducted on the CFHT in early 2004. One of the most notable features of these cluster observations is the fact that they were obtained using CFHT’s wide-field mosaic imager known as “MegaCam”. As shown in Figure 1, MegaCam contains 36 individual CCDs that combine to offer nearly a full 1x1 degree field of view with high angular resolution ($\sim 0.187''$ pixel $^{-1}$ at the f/4 prime focus). Moreover, MegaCam operates with a set of $g'r'i'z'$ filters whose effective wavelengths and bandwidths are very similar to those of the USNO/SDSS. For observations in the UV, however, a slightly different filter than u' is employed; this so-called u^* filter was designed to take advantage of the superb sensitivity of the MegaCam CCDs at short wavelengths along with the reduced atmospheric extinction in the UV at high altitudes.

In order to graphically compare the USNO and MegaCam photometric systems, we present in Figure 2 the spectral coverages of both filter sets. Note that both sets of response

functions presented in the figure are a result of convolving the raw filter profiles with the reflection/transmission characteristics of the telescope optics and the quantum efficiency of the detectors employed at both the USNO and CFHT telescopes². The differences between u^* and u' mentioned above are clearly evident in the plot with the central wavelength of the u^* filter positioned about 200Å *redder* than that of standard u' filter employed at the USNO. As discussed later in this investigation, this fact poses a particular problem in transforming photometry observed in MegaCam’s u^* filter to u' on the standard system. Apart from the differences between u^* and u' , however, the agreement between the remaining four filters seems quite good. The only exceptions are the two z' filters where the USNO version appears to have more response towards longer wavelengths. This difference can be explained by the fact that the both the MegaCam and USNO z' filters are manufactured to have no long wavelength cutoff (see Fukugita et al. 1996). Instead, their redward edges are defined by the long-wavelength quantum efficiency characteristics of the detector employed.

2.1. Observations and Data Reduction

Table 1 presents a list of the dates when data for the program clusters were collected on the CFHT during the 2004A observing semester. The observing run identifications provided in the second column denote blocks of several consecutive nights when the same instrumental setup was in place on the telescope, and all raw science images collected during these blocks were preprocessed using the same run-averaged master bias and flat-field frames. It is important to note that, due to the nature of the “queue-scheduled” mode of observing operations at CFHT, the cluster data were collected on nights when actual sky conditions at the telescope closely matched the tolerances specified in the initial project proposal (i.e., near photometric conditions during dark or gray time with moderately good seeing). As a result, the observations were generally conducted on non-consecutive nights, and a complete set of cluster observations in all five filters may not have been collected on the same night or even during the same observing run (for example, the M 3 data were collected over 4 separate nights spanning 3 different observing runs).

Our goals for this project were to obtain a series of five short- and five long-exposure images in each filter for each cluster in our target list. This not only ensured a good signal-to-noise ratio for stars extending from the tip of the RGB down to a few magnitudes below the

²Electronic versions of tables containing this information for the USNO are available at <http://www-star.fnal.gov/ugriz/Filters/response.html> while analogous data for CFHT’s MegaCam can be found at <http://www.cfht.hawaii.edu/Instruments/Imaging/Megacam/specsinformation.html>

turnoff in each filter, but also allowed a star to be detected multiple times to help improve the precision of its final photometry. Furthermore, the telescope was dithered by a few tens of arcseconds between exposures to allow detection of stars that may have fallen on gaps in the MegaCam mosaic in previous frames. In total, 287 separate MegaCam images in the $u^*g'r'i'z'$ filters was collected over the 12 separate nights listed in Table 1. All but one of these nights were deemed photometric on the basis of the observing logs, observer’s notes, and weather conditions at the Mauna Kea site with atmospheric seeing conditions ranging between $0.54''$ and $1.45''$ (FWHM; median of $\sim 0.93''$) over all nights. Table 2 lists the number of short and long exposure images obtained per filter on a cluster-by-cluster basis. It is worthwhile to note that in addition to the clusters listed in Table 2, the globular cluster M 5 and the open cluster M 67 were included as targets in the observing proposal. However, M 67 was not observed during this period, while only 8 g' frames were taken for M 5. As a result, these two clusters are excluded from consideration for the remainder of the analysis. In addition, the 8 i' images for M 3 obtained during non-photometric conditions were also excluded from the data reductions. This left 271 MegaCam images remaining to be processed in the analysis below.

It is important to note that all of the raw science images acquired for this investigation were preprocessed by CFHT’s Elixir project (Magnier & Cuillandre 2004) prior to their distribution to the principal investigators. This involved the standard steps of overscan correction, bias subtraction, flat-fielding (using run-averaged twilight sky flats), masking of bad pixels, and fringe removal from the i' and z' images. The Elixir project also provided a preliminary astrometric calibration and photometric analysis for each MegaCam image. The latter involved a normalization of the background level in each CCD to enforce a nearly identical instrumental zero-point for all chips and ensure that the final processed data show only small variations from a constant background over the entire mosaic.

As a result of the processing done by Elixir, the data analysis could proceed directly to the extraction of the instrumental PSF photometry from each MegaCam image. In this respect, no attempt was made prior to these reductions either to combine the 36 different CCD images into a single master exposure or to co-add the dithered exposures, but rather the digital images from the 36 individual CCDs were processed separately as if they came from distinct cameras. This was advantageous since the act of assembling multiple CCDs into a large mosaiced image often requires the “resampling” of the individual images to account for subtle chip-to-chip differences in scale and rotation. This type of processing generally requires pixel interpolations and extrapolations that can distort the PSF in certain regions of the mosaic and may lead to spurious photometry for some objects during the PSF fitting.

Since the reduction of the CFHT images was conducted in a manner similar to that

described in Paper I, only a brief review is provided here. First, a UNIX shell script was employed to non-interactively run the PSF-building and star subtraction DAOPHOT/ALLSTAR routines (Stetson 1987; Stetson & Harris 1988) on each individual CCD frame. After star lists and associated instrumental PSF photometry for each frame had been derived, the correction of the relative profile-fitted photometry to a more absolute, aperture-based system was accomplished with concentric aperture growth curves derived using the DAOGROW package (Stetson 1990). Finally, the geometric transformations of the natural (x, y) coordinate system of the individual CCD images to an astrometrically meaningful system (ξ, η) ; see, e.g., Smart 1965) based on the USNOB-1.0 catalog (Monet et al. 2003) was accomplished via a set of third-order polynomials.

2.2. Photometric Calibrations

As a result of the efforts described in Paper I, most star clusters in the CFHT survey contain a sizable number of local standard stars whose magnitudes have been referred to the $u'g'r'i'z'$ system with an accuracy of 1% or better in each filter. Therefore, calibrating the cluster photometry relies solely on comparing the observed instrumental magnitudes for these stars to their counterparts on the standard system in order to solve for the transformation coefficients using robust least-squares analysis. In the beginning stages of the calibration process, each CCD exposure from the mosaic was treated separately. That is, the transformation constants were allowed to be determined freely and independently on the basis of the local standard stars contained in the image. Unfortunately, since the range in air mass spanned by the cluster observations on any given night was typically quite small ($\Delta(\sec z) \lesssim 0.2$), it was soon discovered that the derived extinction coefficients often took on negative values and/or were wildly inconsistent between the different CCD images. Due to these findings, the canonical atmospheric extinction coefficients for Mauna Kea (as determined by the Elixir project) were employed for the calibrations rather than having them computed from the data. That is, all chips are assigned $K_{u^*} = 0.35$, $K_{g'} = 0.15$, $K_{r'} = 0.10$, $K_{i'} = 0.04$, and $K_{z'} = 0.03$ mag per air mass for all photometric nights.

With the extinction coefficients set to constant values for all chips, secondary runs through the calibrations were performed with one less unknown in the transformation equations. Upon completion, a weighted average of the linear color terms was then calculated and imposed as an additional known constant common to all chips for a final calibration run that left only the photometric zero points to be recomputed on a chip-by-chip basis. Given the fact that the spectral response of a telescope/detector system is largely determined by the combined effects of the transmission of the atmosphere, the reflectivity and transmissivity of

the telescope components, and throughput of the filters, it can be expected that chip-to-chip differences in the computed color terms vary by only a few percent (provided that the CCDs are similar in design and the filter is spatially uniform). Indeed, from our own derivation of separate color terms for different chips, we found that the largest variations in the color coefficients between the different chips from any single photometric night amounted to $\sim 4\%$ in the u' filter.

Once the transformation constants from all nights were derived, the best estimates of the calibrated magnitudes for each secondary standard star observed over all 11 photometric nights were then determined. Figures 3 and 4 illustrate the extent to which the cluster data have been placed on the standard system by comparing the $u'g'r'i'z'$ photometry to the mean calibrated photometry for the secondary standards stars. The small, gray data points in each panel represent the difference between the magnitudes on the standard $u'g'r'i'z'$ system and the *mean* magnitude as a function of their respective magnitudes in Figure 3 and $(g' - i')$ color in Figure 4. To better aid in the detection of any systematic trends not immediately evident to the eye, each large dot represents the unweighted median difference for stars in intervals of 0.5 in magnitude or 0.25 mag in $(g' - i')$ color with their corresponding error bars providing a robust measure of the spread in the residuals within each bin (i.e., $(\pi/2)^{1/2}$ times the mean absolute deviation).

A few features in both figures warrant detailed explanations. First, there is a noticeable excess of scatter in the data points towards positive values in each panel of Figure 3; this seems to indicate that a sizable fraction of the secondary standards with $r' \gtrsim 15$ have had their magnitudes on the standard system measured too bright compared to the values derived here. The most likely explanation for this effect is the fact that these standards are located closer to cluster cores and hence their photometry in the DAO images has been contaminated by light from nearby stars. This would serve to make the secondary standards appear brighter than they actually are. As mentioned in Paper I, since atmospheric seeing conditions averaged around $3 - 4''$ at the DAO for the establishment of the secondary standards, it is reasonable to expect a higher probability of spurious photometry resulting from the effects of crowding in the DAO images compared to the CFHT observations (with average seeing values of $\sim 1.0''$). To better test this statement, we have produced plots similar to those in Figures 3 and 4 where stars are culled based on how crowded they are in the DAO images as derived by *sep* index (a detailed definition of this parameter is presented below). While we do not present these plots here, we did find that the more crowded stars tended to exhibit more scatter towards positive residual values as well as larger means and standard deviations when compared to plots that considered only less crowded stars. Hence, we strongly feel that our derived photometric transformations are sufficient to transform the observed MegaCam photometry to the standard system based on the fact that the median magnitude differences

tend to lie within 0.01 mag of zero difference over the entire ranges in g' , r' , i' , and z' , and the lines corresponding to zero difference tend to pass through the densest parts of the point distributions.

Secondly, the situation with the u' magnitude differences plotted as a function of color in the top panel of Figure 4 appears quite troublesome. In particular, there is considerable disagreement in the residuals towards bluer and redder colors which would seem to suggest that the use of a single linear color term in the transformation equations is inadequate to account for the bandpass mismatch between the u^* and u' filters. As mentioned above, CFHT’s u^* filter was constructed to be substantially different than the u' filter in order to take advantage of the good UV sensitivity of MegaCam and reduced atmospheric extinction at short wavelengths atop Mauna Kea. The effective wavelength of the u^* filter is about 200Å redder than that of u' , and, as shown in Figure 2, this places most of the u^* response *redward* of the Balmer discontinuity at 3700Å; this has profound implications for transforming the observed u^* magnitudes for B- and A-type stars (i.e., those with the largest Balmer jumps) to the standard system.

2.3. Transforming u^* to u'

The deviations shown in the top panel of Figure 4 for $\Delta u'$ appear to indicate that the transformation of MegaCam’s u^* to u' is more complex than can be accounted for using a simple linear color term. As a result, we have endeavored to derive a more realistic higher-order polynomial transformation that would better convert MegaCam’s u^* photometry to u' on the standard system. To keep this derivation as empirically-based as possible, we employed our own photometric data as well as the colors and magnitudes computed by convolving the filter transmission functions for both the standard $u'g'r'i'z'$ and MegaCam’s $u^*g'r'i'z'$ systems (c.f. Figure 2) with the spectral energy distributions for real stars. For the latter, we opted to use the SEDs presented in the Gunn & Stryker (1983) spectrophotometric catalog that cover a wide range in luminosity and spectral class in order to better investigate the difference between u^* and u' photometry for different stellar types. When the differences between the “computed” u^* and u' magnitudes are compared against $(g' - i')$, as shown in Figure 5, we see that indeed there is a rather complex behavior in the residuals that appears to coincide quite well with the residuals shown in the top panel of Figure 4 (the gray squares with error bars denote the same median points plotted in Figure 4). While it would appear that the dwarfs and giants follow a slightly different trend towards redder colors (i.e., $(g' - i') \gtrsim 1.0$), we have decided to find a single, multi-order function that would best correct the u^* photometry for most stellar types. Consequently, the solid line plotted in

the figure indicates the third-order polynomial we have fitted to both sets of data to better define the transformation between u^* and u' . Note that this fit is only valid over the range $-0.5 < (g' - i') < 3.5$ and is not intended to correct the u^* photometry for extremely blue or red stars.

To test the quality of this new non-linear transformation between u^* and u' , Figure 6 presents a comparison between various VandenBerg et al. (2006) isochrones with the denoted ages and metallicities (as plotted left to right in the figure) that have been transformed to the $[(u' - g'), M_{r'}]$ plane using color-temperature relations computed from the ATLAS9 synthetic spectra presented by Castelli et al. (1997). The left-hand panel employs the linear color terms that were initially derived to transform the MegaCam photometry to the standard system, and it shows that the two sets of isochrones are in considerable disagreement in a number of different locations due to the mismatch between the u^* and u' filters, most notably in the turnoff region for metal-poor stars, and the RGB and main sequence regions for more metal-rich stars. The right-hand panel, on the other hand, plots isochrones where u^* has been corrected using the third-order function shown in Figure 5. Reassuringly, the new nonlinear transformation seems to provide theoretical loci in the region $0.0 \gtrsim (u' - g') \gtrsim 3.0$ that are in quite good agreement with those on the standard system, and, with a few exceptions discussed below, both sets of isochrones overlap each other to within 0.01 mag over the entire range in magnitude. This fact bodes well for our derivation of the fiducial cluster sequences in u' since the stars that define RGB, SGB, turnoff, and upper-MS loci for all clusters in the survey fall within this color range.

In regards to the few remaining obvious differences between the two theoretical loci in the right-hand panel for the upper-RGB for the most metal-poor isochrone and the lower-MS for the most metal-rich, they would appear to indicate that our polynomial relation is unable to correct the u^* magnitudes for *all* types of stars (in particular, those stars that lie at the extremes of luminosity, color, and/or metallicity). Unfortunately, as far as we are aware, there does not exist a sufficient database of stars with varying metallicities, temperatures, and/or luminosities that have been observed in both the u^* and u' filters to conduct a more rigorous investigation into the differences between these two filters for a wide-variety of stellar types. Also, it is important to stress, that the transformations between u^* and u' that we have derived here are invalid for blue horizontal branch stars or other hot stars, such as blue post-AGB stars, sdB stars, white dwarfs, or some blue stragglers. Although we are quite confident that the fiducials we derive below are accurately calibrated to the standard system for the g' , r' , i' , and z' filters, we strongly advise the reader to use caution when employing the sequences that include u' filter for the interpretation of stellar photometry, especially for metal-poor giants or metal rich dwarfs, due to the simple fact that the fiducials may not be adequately transformed to u' on the standard system for these types of stars.

3. The Cluster Photometry

The transformation terms computed during the calibration to the standard $u'g'r'i'z'$ system described in the previous section were subsequently applied to the instrumental magnitudes that were derived for all detected objects in every CCD image for each cluster field. Simultaneously, the zero points between the relative profile-fitting magnitude system and the standard one were redetermined by direct comparison to the local secondary standards within each cluster field on a frame-by-frame basis. This final step in the reduction process compensates for uncertainties caused by short term fluctuations in the extinction or errors in the aperture corrections. While this does nothing to improve the absolute calibration of the photometry to the standard system in the mean, it does improve the frame-to-frame repeatability of the measurements by ensuring that the photometry from each image is now referred to a common magnitude zero point defined by the local secondary standards. In addition, the transformation of the natural (x, y) coordinates of the stars in each image to an astrometrically meaningful system based on the USNOB-1.0 catalog facilitates the matching of stars from different chips and different exposures and results in a single master star list for the entire field surrounding each cluster.

3.1. Refining the Sample

Given that we have on hand approximately 16.9 million individual magnitude and position measurements derived for some 650,000 distinct objects in 5 different clusters, it is inevitable that a sizable number of these detections will be non-stellar objects (e.g., background galaxies, cosmic rays, satellite or meteor trails, etc.) or image blemishes (e.g., defective pixels, diffraction spikes, etc.). Moreover, when dealing with crowded cluster fields such as these, the photometry for a significant fraction of the legitimate stars will undoubtedly be contaminated by light from neighboring objects even under the most ideal seeing conditions. As a result, when the cluster photometry is plotted on color-magnitude or color-color diagrams for the purpose of analysis, these spurious objects and crowded stars may contribute increased scatter or broadening of the primary cluster sequences, and it is better to exclude them from consideration when deriving the fiducials. While it is obviously not feasible to censor problematic measurements by hand, the various programs that have been used to extract the PSF instrumental photometry from the CCD images output certain image-quality and data-reliability indices that can be used to reject spurious detections or non-stellar objects from consideration. In addition to these indices, the discussion below describes the mechanics of the so-called “separation index” (*sep*; see Stetson et al. 2003) that is quite effective in culling severely crowded stars from the cluster data sets.

In brief, the definition of the separation index is based on the fact that the typical seeing profile for each star in a particular image is well approximated by the Moffat function (Moffat 1969):

$$S(r) \propto \frac{F}{[1 + (r/r_o)^2]^\beta}, \quad (1)$$

where r is the distance from the star’s centroid, r_o is some characteristic radius that can be related to FWHM of the stellar brightness profile, F is just the stellar flux determined from $F \propto 10^{-0.4m}$; where m is the apparent magnitude, $S(r)$ is the surface brightness of the stellar profile at radius r , and β is a parameter that governs the shape of the stellar profile. Based on this definition, if one assumes a reasonable value for β (typically 1.5–2.5 for stellar profiles in digital images) and FWHM for the seeing value, it is a simple matter to compute the surface brightness produced by a particular star with both an apparent magnitude m and a centroid position at any point in the field. Based on this definition, the *sep* index for any given star can be mathematically expressed as:

$$sep_i = \frac{S_i(0)}{\sum_{j \neq i} S_j(r_j)}. \quad (2)$$

Here $S_i(0)$ is the surface brightness at the centroid of the star in question and $S_j(r_j)$ is the surface brightness contribution from the j^{th} neighboring star situated at a distance r_j away.

The computation of the *sep* index for the 5 different cluster data sets assumes the typical values of FWHM = 1.0'' and $\beta = 2$ and uses the apparent r' magnitude to define the fluxes for the individual stars. In order to save computational time, the determination of *sep* for any particular star in the field considers contributions only from those stars lying within 10 times the assumed FWHM. The top panel of Figure 7 shows the plot of the derived *sep* index versus apparent r' magnitude for stars in M 13. As evidenced by the higher concentration of points at increasing magnitudes, fainter stars are more susceptible to contamination by light from neighboring stars in the field than bright ones. Since the M 13 turnoff corresponds to $r' \sim 18.6$, the scattering of points to brighter magnitudes and higher *sep* values primarily correspond to stars lying on the RGB and HB of this cluster. Based on examinations of the cluster CMDs using different *sep* cuts, it was determined that stars with *sep* > 3.5 (i.e., stars where the summed wings of all other stars in the field amount to no more than $\sim 4\%$ of the central surface brightness of the star itself) produced the most well-defined cluster sequences. Therefore, the remainder of this discussion only considers those stars with *sep*

values above 3.5.

During the process of deriving PSF magnitudes the DAOPHOT/ALLSTAR software computes two image-quality indices known as χ and *sharp* for every detected object in a CCD image. In the final reduction of all the data for a particular cluster, the individual χ and *sharp* measurements for each star are then averaged and reported in the data tables. Briefly, χ is simply a measure of the agreement between the object’s observed brightness profile and the derived PSF model (i.e., the quality of the fit between the model PSF and the object). As shown in the middle panel of Figure 7, the χ values for the vast majority of objects with $sep > 3.5$ in M13 tend to cluster around $\chi \approx 1$ over the entire magnitude range which would indicate that they are legitimate stars. Those at larger χ values, on the other hand, are most likely either non-stellar objects or stars whose brightness profiles are corrupted by image defects or diffraction spikes. Stars lying above the solid curve shown in the same panel are excluded on the basis of the χ values. Finally, a plot of the *sharp* index versus apparent r' magnitude in the bottom panel of Figure 7 shows that real stars have a propensity to hover in a narrow range centered on zero. This is due to the fact that the *sharp* index measures the degree to which an object’s intrinsic angular radius differs from that of the model PSF. Therefore, detections with large positive *sharp* values have larger characteristic radii compared to the PSF model and are most likely resolved galaxies, while those with significantly negative *sharp* values have apparent radii smaller than the seeing profile, and thus are unlikely to be astronomical objects viewed through the atmosphere and telescope optics; they probably correspond to an image blemishes or cosmic rays. As a result, one can safely assume that objects with $|sharp| < 1$ have a high degree of probability of being real stars.

To demonstrate the effectiveness of the χ , *sharp*, and *sep* indices in culling crowded stars and spurious objects from the photometry lists and producing extremely well-defined cluster sequences, Figure 8 shows two CMDs for M13 with those stars that survived the cuts plotted in the left-hand panel and those that did not in the right. Note the well-defined and very tight cluster sequences extending from the RGB to the lower main sequence in the left-hand panel. In contrast, stars that were excluded in the right-hand panel result in a quite diffuse and noisy main sequence, turnoff, and lower-RGB regions due largely to the effects of crowding. It is important to mention that while the stars plotted in the left panel do not represent a *complete* sample of all the cluster members, they do provide a suitable *representative* sample for the derivation of the fiducial sequences.

3.2. Defining the Fiducials

With objects from each of the cluster data files rejected or accepted according to the cuts in χ , *sharp*, and *sep* mentioned above, the definition of the fiducial sequences from the cluster photometry proceeds by defining the ridge lines of the stellar locus in color-magnitude space. Due to the various possible combinations of different colors and magnitudes that are available to plot a cluster’s CMD, the r' magnitude was adopted as the primary ordinate against which the median colors were defined since the cluster loci are rarely double valued in r' , and the level of completeness at faint magnitudes is the best for r' . Therefore, each ridge line is created by determining the median color of stars that lie within different r' magnitude bins. The size of these bins is arbitrarily adjusted along the cluster locus to include a sufficient number of stars to define a median color. For example, larger magnitude bins are defined in parts of the CMD where the photometric scatter is larger at the faint end and where the number of stars is scarce at the bright end. Smaller bins are employed for areas of the cluster loci with large curvature and numerous stars (e.g., between the turnoff and base of the RGB). Outlying stars are iteratively clipped during the determination of the median color to ensure that the ridge line is not significantly skewed. While this technique seemed to work quite well, there were some regions of the CMD where the number of stars is just too small, the scatter in the sequences is too large, or the cluster locus is double valued (i.e., the subgiant branch of NGC 6791) for an accurate median color to be defined; in these cases the location of the points defining the ridge lines are determined by eye estimation.

Figures 9 through 13 present the various CMDs of each cluster in the sample along with their associated ridge lines spanning the MS, SGB, and RGB (tabulated in Tables 3-7). It is important to note that the photometry for each cluster has been censored according to the same χ , *sharp*, and *sep* cuts mentioned above before plotting. In addition, only those stars that lie within a radius of $2.5'$ and $5.0'$ of the centers of M 71 and NGC 6791, respectively, have been plotted to help reduce field star contamination in their CMDs. These imposed cuts appear to have been quite successful in yielding extremely well-defined and tight loci of stars extending from the upper-RGBs down to approximately 4 magnitudes below the turnoff points.

4. Summary

Using high-quality, homogeneous observations obtained with the wide-field MegaCam imager on the 3.6m Canada-France-Hawaii Telescope, we have derived fiducial stellar population sequences for the Galactic star clusters M 92, M 13, M 3, M 71, and NGC 6791 in the $u'g'r'i'z'$ photometric system. These sequences, which span a wide range in both metallicity

and magnitude, have been accurately calibrated to within 1% of the standard $u'g'r'i'z'$ system using a set of secondary standard stars derived in Paper I. As a result of our efforts, we anticipate that these fiducial sequences will serve as valuable tools for the interpretation of other stellar population investigations involving the $u'g'r'i'z'$ bandpasses by virtue of the fact that they represent a set of empirical isochrones for both metal-poor and metal-rich stars having wide-ranging physical parameters. Indeed, a preliminary set of the fiducials presented in this work has already been employed in the interpretation of CMDs for a number of newly discovered Milky Way satellites (see, for example, Belokurov et al. 2006, 2007a,b).

In addition to the usefulness of these fiducial sequences for the interpretation of observed data, they also provide an excellent test of the accuracy of color-temperature relations and bolometric corrections that have been derived from model atmospheres and synthetic spectra. In a future paper (J. L. Clem et al. 2008, in preparation) we intend to perform tests of such synthetic color and magnitude transformations by comparing isochrones models to the fiducials derived here. Our aim is to assess the quality of the color-temperature relations and bolometric corrections in providing isochrones that can reproduce the observed cluster photometry when reasonable estimates of the cluster reddening, metallicity, and distance are assumed, as well as test their consistency when isochrone fits to the $u'g'r'i'z'$ photometry are compared to those in other photometric systems (e.g., $BV(RI)_C$ and $uvby$).

It is important for the reader to note, however, that the fiducials derived in this investigation are presented on the $u'g'r'i'z'$ system and *not* on the natural photometric system of the 2.5 m SDSS survey telescope (i.e., the $ugriz$ system). Subtle differences exist between the two systems such that photometry reported on both systems for an identical stellar sample can differ systematically by as much as a few hundredths of a magnitude in some filters. Therefore, we caution against using these fiducials to interpret and/or analyze $ugriz$ photometry from the SDSS without first applying appropriate transformation relations (see Tucker et al. 2006). Although these transformations may not be appropriate for stars with strong emission features in their spectra or stars with extreme colors (i.e., later than M0 spectral class), we expect they are good enough to transform the fiducials presented here on the $u'g'r'i'z'$ system to the SDSS 2.5 m $ugriz$ system, while keeping the uncertainties in the photometric zero points on the AB system (see Oke & Gunn 1983) to within a few percent.

This work has been supported by an Operating Grant to D. A. V. from the Natural Sciences and Engineering Research Council of Canada. This paper was prepared with support from NSF grant AST 05-03871 to A. U. Landolt.

REFERENCES

- Abazajian, K., et al. 2003, *AJ*, 126, 2081
- Belokurov, V., et al. 2006, *ApJ*, 647, L111
- Belokurov, V., et al. 2007a, *ApJ*, 654, 897
- Belokurov, V., et al. 2007b, *ApJ*, 658, 337
- Brown, T. M., et al. 2005, *AJ*, 130, 1693
- Castelli, F., Gratton, R. G., & Kurucz, R. L. 1997, *A&A*, 318, 841
- Clem, J. L., VandenBerg, D. A., & Stetson, P. B. 2007, *AJ*, 134, 1890 (Paper I)
- Fukugita, M., Ichikawa, T., Gunn, J. E., Doi, M., Shimasaku, K., & Schneider, D. P. 1996, *AJ*, 111, 1748
- Gunn, J. E., & Stryker, L. L. 1983, *ApJS*, 52, 121
- Magnier, E. A., & Cuillandre, J.-C. 2004, *PASP*, 116, 449
- Moffat, A. F. J. 1969, *A&A*, 3, 455
- Monet, D. G., et al. 2003, *AJ*, 125, 984
- Oke, J. B., & Gunn, J. E. 1983, *ApJ*, 266, 713
- Smart, W. M. 1965, Cambridge: University Press, 1965/71, 5th ed.
- Smith, J. A., et al. 2002, *AJ*, 123, 2121
- Stetson, P. B. 1987, *PASP*, 99, 191
- Stetson, P. B. 1990, *PASP*, 102, 932
- Stetson, P. B., & Harris, W. E. 1988, *AJ*, 96, 909
- Stetson, P. B., Bruntt, H., & Grundahl, F. 2003, *PASP*, 115, 413
- Tucker, D. L., et al. 2006, *Astronomische Nachrichten*, 327, 821
- VandenBerg, D. A., Bergbusch, P. A., & Dowler, P. D. 2006, *ApJS*, 162, 375

Table 1. Observing Log for the CFHT Star Cluster Survey

UT Dates	Run ID	u^*	g'	r'	i'	z'	Clusters Observed	Photometric?
2004-05-13	04AM04	7	0	0	0	0	M 92	Y
2004-05-23	04AM05	20	0	0	0	10	M 3, M 92	Y
2004-06-10	04AM06	0	10	10	10	0	M 92	Y
2004-06-11		5	10	10	10	0	M 3	Y
2004-06-14		0	0	0	8	0	M 3	N
2004-06-19		0	10	10	10	0	NGC 6791	Y
2004-07-07	04AM07	8	6	0	0	0	M 13, NGC 6791	Y
2004-07-08		0	10	10	10	0	M 71	Y
2004-07-10		10	0	0	0	12	NGC 6791	Y
2004-07-13		10	0	0	0	10	M 71	Y
2004-07-16		10	10	10	10	10	M 13	Y
2004-07-17		3	8	0	0	0	M 3, M 5	Y
Totals		73	64	50	58	42		

Table 2. Number of $u^*g'r'i'z'$ observations per cluster

Cluster	u^*	g'	r'	i'	z'
M 92	17	10	10	10	10
M 13	10	16	10	10	10
M 3	18	10	10	18	0
M 71	10	10	10	10	10
NGC 6791	18	10	10	10	12
Totals	73	64	50	58	42

Table 3. Ridge lines for the globular cluster M 92.

u'	g'	r'	i'	z'
15.550	12.650	11.500	10.992	10.710
15.336	12.952	12.000	11.589	11.363
15.362	13.335	12.500	12.139	11.946
15.541	13.746	13.000	12.670	12.495
15.809	14.184	13.500	13.200	13.040
16.143	14.634	14.000	13.724	13.575
16.502	15.093	14.500	14.245	14.107
16.876	15.554	15.000	14.762	14.633
17.275	16.023	15.500	15.278	15.159
17.690	16.497	16.000	15.790	15.681
18.120	16.976	16.500	16.300	16.200
18.560	17.458	17.000	16.811	16.720
18.735	17.648	17.200	17.016	16.928
18.896	17.828	17.400	17.221	17.140
19.014	17.995	17.600	17.438	17.368
19.108	18.145	17.800	17.668	17.614
19.220	18.287	18.000	17.898	17.867
19.374	18.453	18.200	18.119	18.101
19.549	18.638	18.400	18.329	18.320
19.740	18.835	18.600	18.529	18.522
19.939	19.038	18.800	18.725	18.716
20.147	19.248	19.000	18.919	18.907
20.359	19.460	19.200	19.112	19.095
20.576	19.675	19.400	19.302	19.280
20.799	19.894	19.600	19.493	19.464
21.031	20.117	19.800	19.682	19.646
21.274	20.343	20.000	19.869	19.824
21.947	20.916	20.500	20.331	20.264
22.732	21.509	21.000	20.787	20.693
23.618	22.110	21.500	21.237	21.113
24.516	22.729	22.000	21.683	21.527
...	23.356	22.500	22.126	21.933
...	23.973	23.000	22.572	22.345

Table 4. Ridge lines for the globular cluster M 13.

u'	g'	r'	i'	z'
16.300	12.630	11.300	10.760	10.411
15.925	12.871	11.800	11.340	11.077
15.830	13.233	12.300	11.902	11.690
15.863	13.624	12.800	12.447	12.266
16.025	14.050	13.300	12.980	12.815
16.279	14.494	13.800	13.508	13.355
16.584	14.947	14.300	14.032	13.889
16.921	15.407	14.800	14.550	14.416
17.282	15.870	15.300	15.065	14.942
17.672	16.338	15.800	15.576	15.460
18.089	16.809	16.300	16.086	15.977
18.520	17.286	16.800	16.594	16.491
18.777	17.574	17.100	16.900	16.800
18.937	17.761	17.300	17.105	17.007
19.063	17.939	17.500	17.312	17.223
19.117	18.090	17.700	17.542	17.479
19.160	18.222	17.900	17.778	17.736
19.292	18.385	18.100	17.994	17.965
19.465	18.569	18.300	18.203	18.181
19.655	18.764	18.500	18.406	18.385
19.861	18.970	18.700	18.605	18.583
20.075	19.179	18.900	18.801	18.774
20.293	19.390	19.100	18.995	18.965
20.523	19.607	19.300	19.187	19.150
20.764	19.829	19.500	19.378	19.336
21.017	20.052	19.700	19.567	19.519
21.290	20.278	19.900	19.755	19.699
21.902	20.745	20.300	20.124	20.050
22.777	21.343	20.800	20.579	20.477
23.764	21.963	21.300	21.027	20.886
...	22.604	21.800	21.462	21.279
...	23.265	22.300	21.891	21.667
...	23.906	22.800	22.324	22.059
...	24.449	23.300	22.784	22.473

Table 5. Ridge lines for the globular cluster M 3.

u'	g'	r'	i'	z'
17.220	13.300	12.000	11.420	...
16.588	13.558	12.500	12.054	...
16.490	13.918	13.000	12.617	...
16.566	14.310	13.500	13.162	...
16.751	14.733	14.000	13.695	...
17.003	15.175	14.500	14.219	...
17.290	15.626	15.000	14.739	...
17.611	16.084	15.500	15.255	...
17.985	16.555	16.000	15.770	...
18.386	17.028	16.500	16.285	...
18.810	17.507	17.000	16.797	...
19.244	17.987	17.500	17.308	...
19.418	18.179	17.700	17.511	...
19.573	18.367	17.900	17.716	...
19.695	18.546	18.100	17.929	...
19.714	18.679	18.300	18.159	...
19.752	18.806	18.500	18.403	...
19.898	18.975	18.700	18.618	...
20.077	19.164	18.900	18.824	...
20.274	19.365	19.100	19.025	...
20.481	19.571	19.300	19.224	...
20.693	19.782	19.500	19.417	...
20.916	19.997	19.700	19.609	...
21.144	20.214	19.900	19.799	...
21.387	20.436	20.100	19.988	...
21.641	20.660	20.300	20.176	...
21.920	20.889	20.500	20.364	...
22.696	21.473	21.000	20.824	...
23.587	22.072	21.500	21.277	...
24.491	22.698	22.000	21.720	...
...	23.350	22.500	22.154	...
...	24.018	23.000	22.582	...

Table 6. Ridge lines for the globular cluster M 71.

u'	g'	r'	i'	z'
17.260	13.047	11.500	10.646	10.146
16.920	13.344	12.000	11.360	10.973
16.776	13.703	12.500	11.934	11.607
16.863	14.102	13.000	12.489	12.201
17.046	14.519	13.500	13.036	12.775
17.283	14.953	14.000	13.561	13.321
17.561	15.407	14.500	14.077	13.853
17.877	15.871	15.000	14.588	14.377
18.233	16.337	15.500	15.095	14.893
18.633	16.813	16.000	15.601	15.405
19.062	17.295	16.500	16.106	15.913
19.232	17.489	16.700	16.309	16.116
19.403	17.681	16.900	16.519	16.329
19.518	17.856	17.100	16.763	16.587
19.397	17.886	17.200	16.894	16.743
19.285	17.932	17.300	17.010	16.876
19.294	18.011	17.400	17.117	16.993
19.448	18.193	17.600	17.320	17.204
19.640	18.389	17.800	17.520	17.405
19.855	18.594	18.000	17.717	17.601
20.086	18.806	18.200	17.912	17.793
20.337	19.022	18.400	18.106	17.981
20.609	19.245	18.600	18.297	18.165
20.893	19.470	18.800	18.487	18.347
21.193	19.697	19.000	18.674	18.525
22.029	20.287	19.500	19.132	18.959
22.977	20.908	20.000	19.576	19.370
24.021	21.571	20.500	20.001	19.753
25.075	22.245	21.000	20.421	20.123
...	22.883	21.500	20.835	20.477
...	23.480	22.000	21.240	20.826
...	24.009	22.500	21.632	21.188
...	24.509	23.000	22.132	21.685

Table 7. Ridge lines for the open cluster NGC 6791.

u'	g'	r'	i'	z'
...	14.514	13.100	12.370	11.906
...	14.898	13.600	13.057	12.690
...	15.314	14.100	13.632	13.325
...	15.745	14.600	14.176	13.915
...	16.186	15.100	14.711	14.481
...	16.640	15.600	15.237	15.029
...	17.106	16.100	15.752	15.556
...	17.577	16.600	16.259	16.072
...	17.765	16.800	16.461	16.276
...	17.946	17.000	16.665	16.482
...	18.032	17.120	16.801	16.626
...	17.966	17.120	16.833	16.687
...	17.842	17.060	16.803	16.679
...	17.771	17.050	16.814	16.709
...	17.885	17.200	16.979	16.885
...	18.076	17.400	17.182	17.089
...	18.281	17.600	17.382	17.289
...	18.495	17.800	17.579	17.483
...	18.715	18.000	17.773	17.673
...	18.940	18.200	17.965	17.858
...	19.166	18.400	18.154	18.040
...	19.402	18.600	18.339	18.214
...	20.014	19.100	18.794	18.638
...	20.658	19.600	19.227	19.031
...	21.311	20.100	19.629	19.387
...	21.942	20.600	20.008	19.707
...	22.525	21.100	20.365	19.996
...	23.048	21.600	20.714	20.276
...	23.546	22.100	21.057	20.541
...	24.033	22.600	21.400	20.806
...	24.522	23.100	21.768	21.108

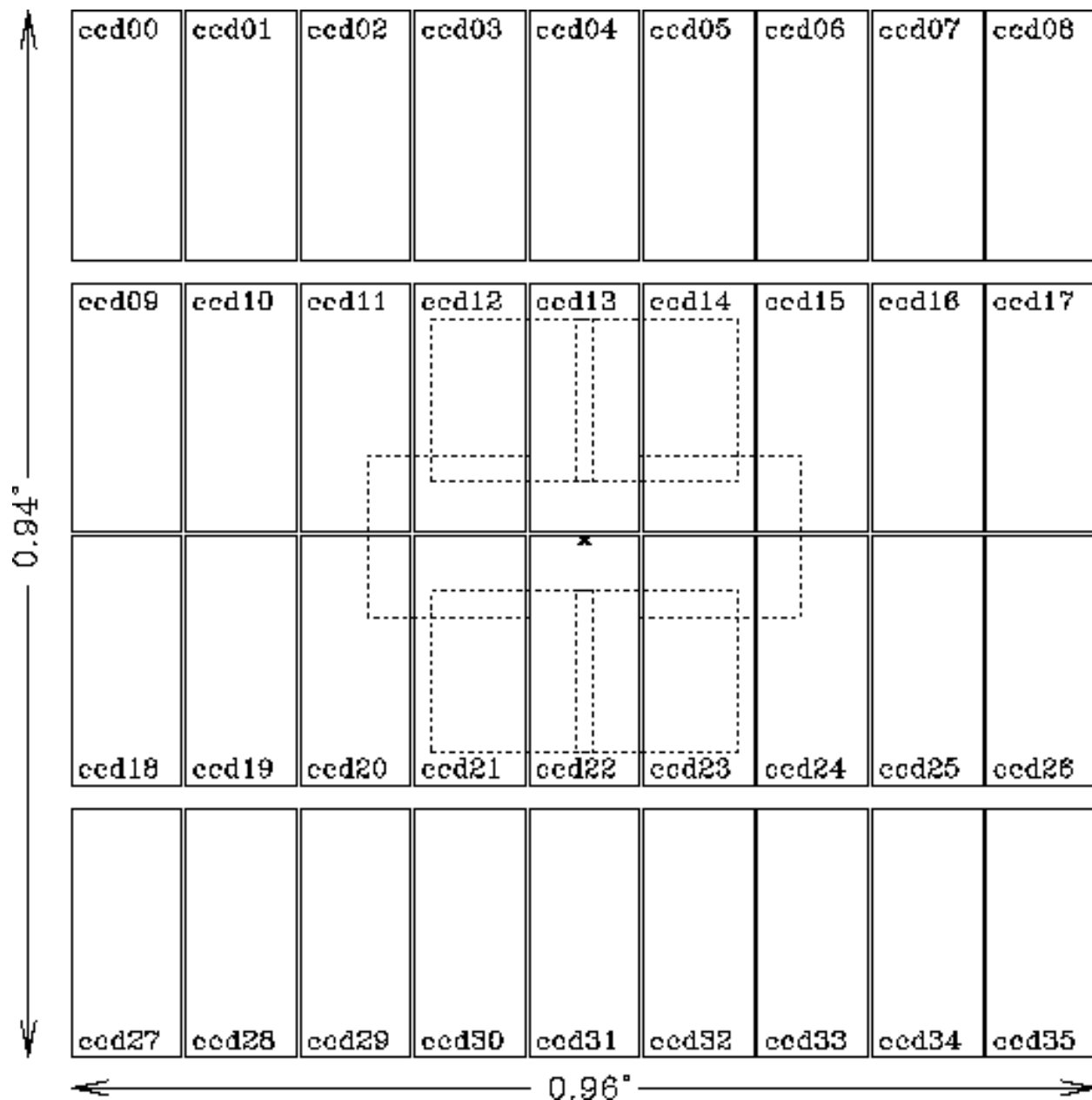


Fig. 1.— Schematic showing the layout of the 36 individual CCD chips in the MegaCam mosaic camera. Each chip measures 2048×4612 pixels and projects to $\sim 6.4 \times 14.4'$ at the CFHT $f/4$ prime focus resulting in a full field of $\sim 0.96 \times 0.94$ degrees for the entire mosaic. The cross near the center of the mosaic (located $\sim 14''$ below the top of ccd22) corresponds to the location of the optical axis of the telescope in the focal plane. The boxes denoted by dotted lines indicate the approximate locations of the 6 fields containing the secondary $u'g'r'i'z'$ standards (cf. Figure 2 in Paper I).

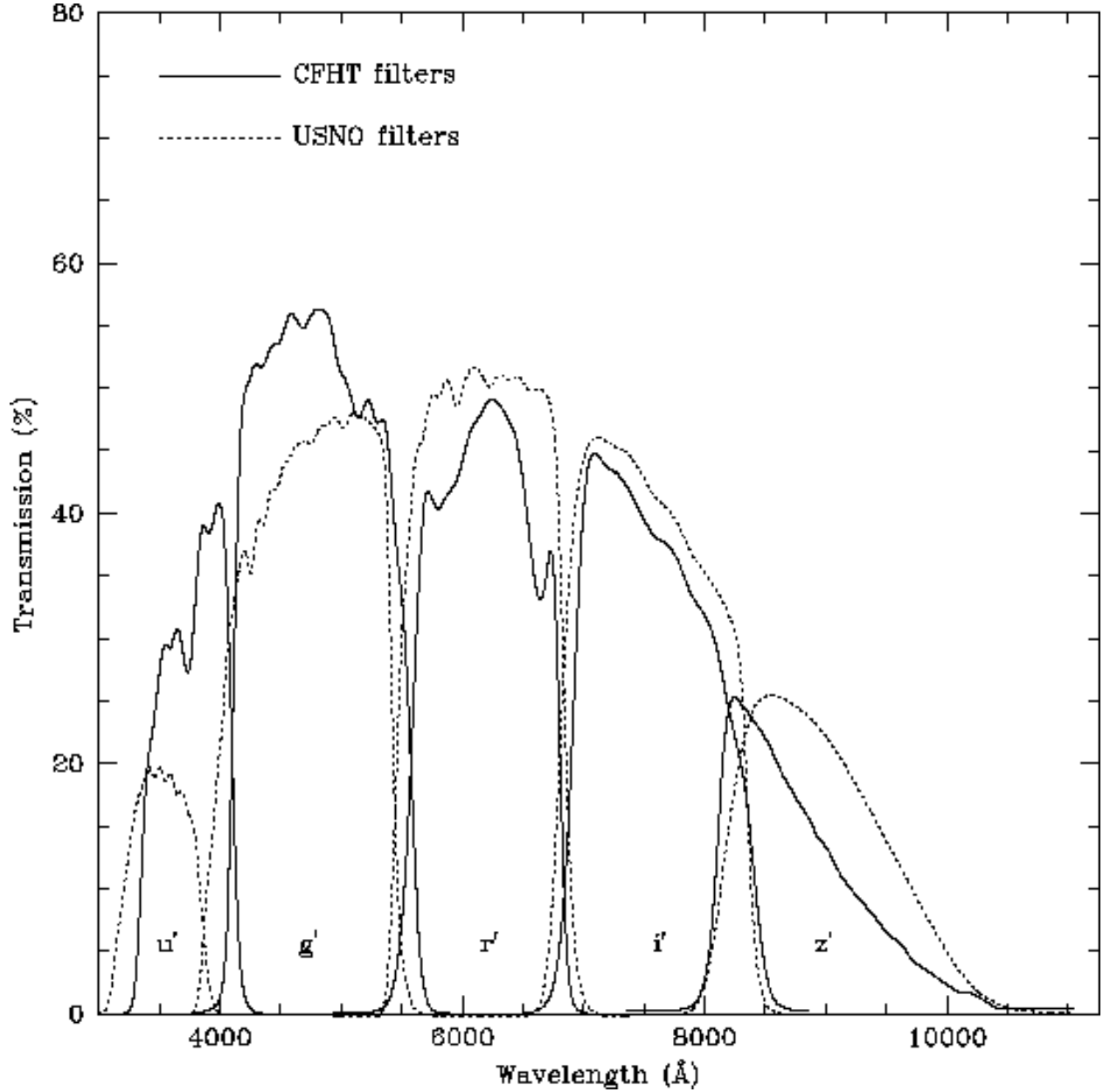


Fig. 2.— Spectral coverages of the CFHT/MegaCam $u^*g'r'i'z'$ and USNO $u'g'r'i'z'$ filter sets. Note that the effective wavelength of MegaCam's u^* filter is shifted redward by about 200\AA compared to the u' filter.

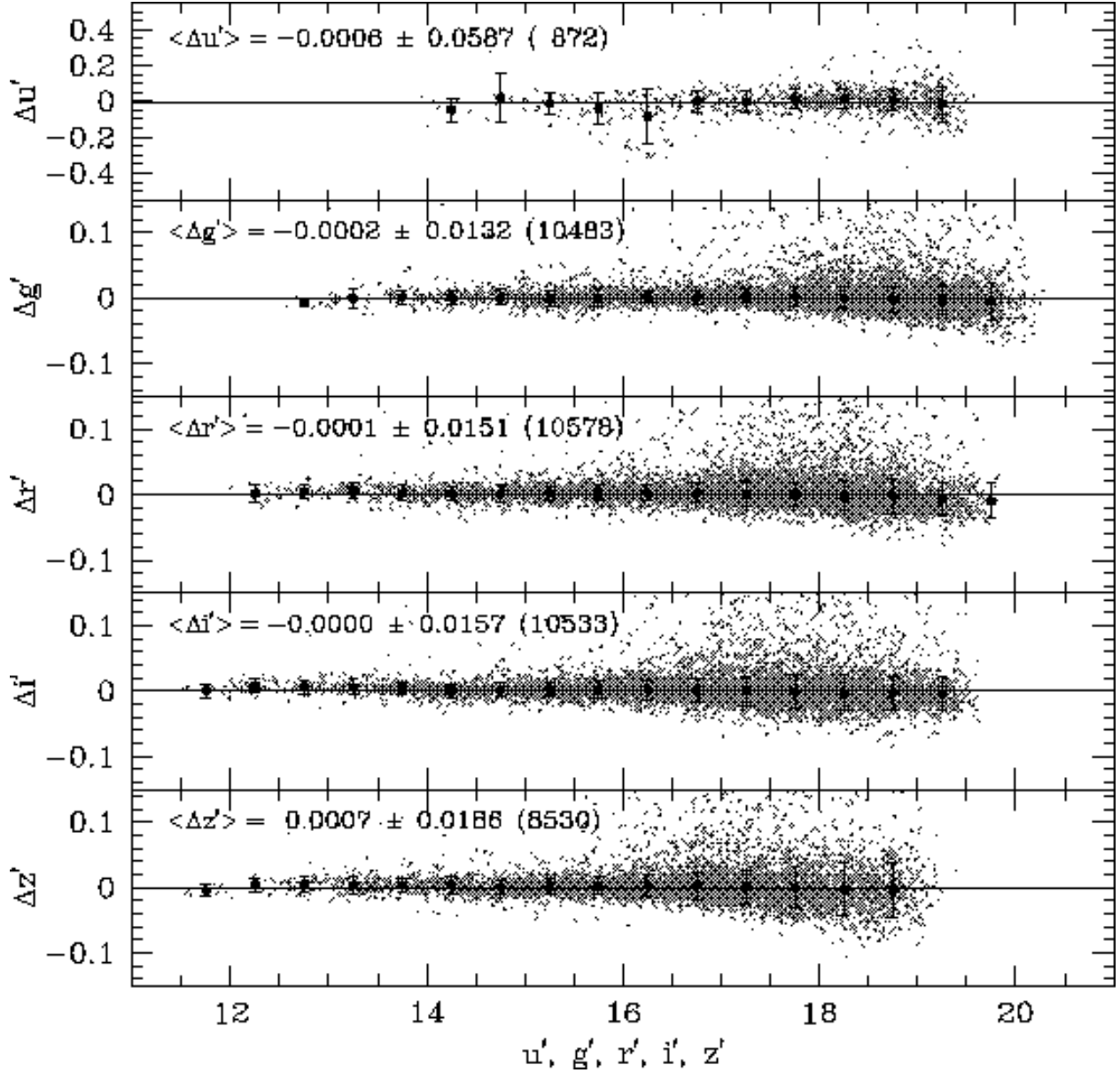


Fig. 3.— Plot of the photometric differences for stars observed over the 11 photometric nights on CFHT that also appear in the database of secondary $u'g'r'i'z'$ standards derived in Paper I. Each Δmag is plotted against its respective magnitude on the standard system. The gray dots represent individual secondary standard stars in common between the two data sets while the large black circles designate the median difference in bins of 0.5 mag. The error bars associated with the median values correspond to a robust measure of the dispersion in the differences within each bin. The mean Δmag differences, associated standard deviations, and number of stars used to define the mean are denoted in each panel.

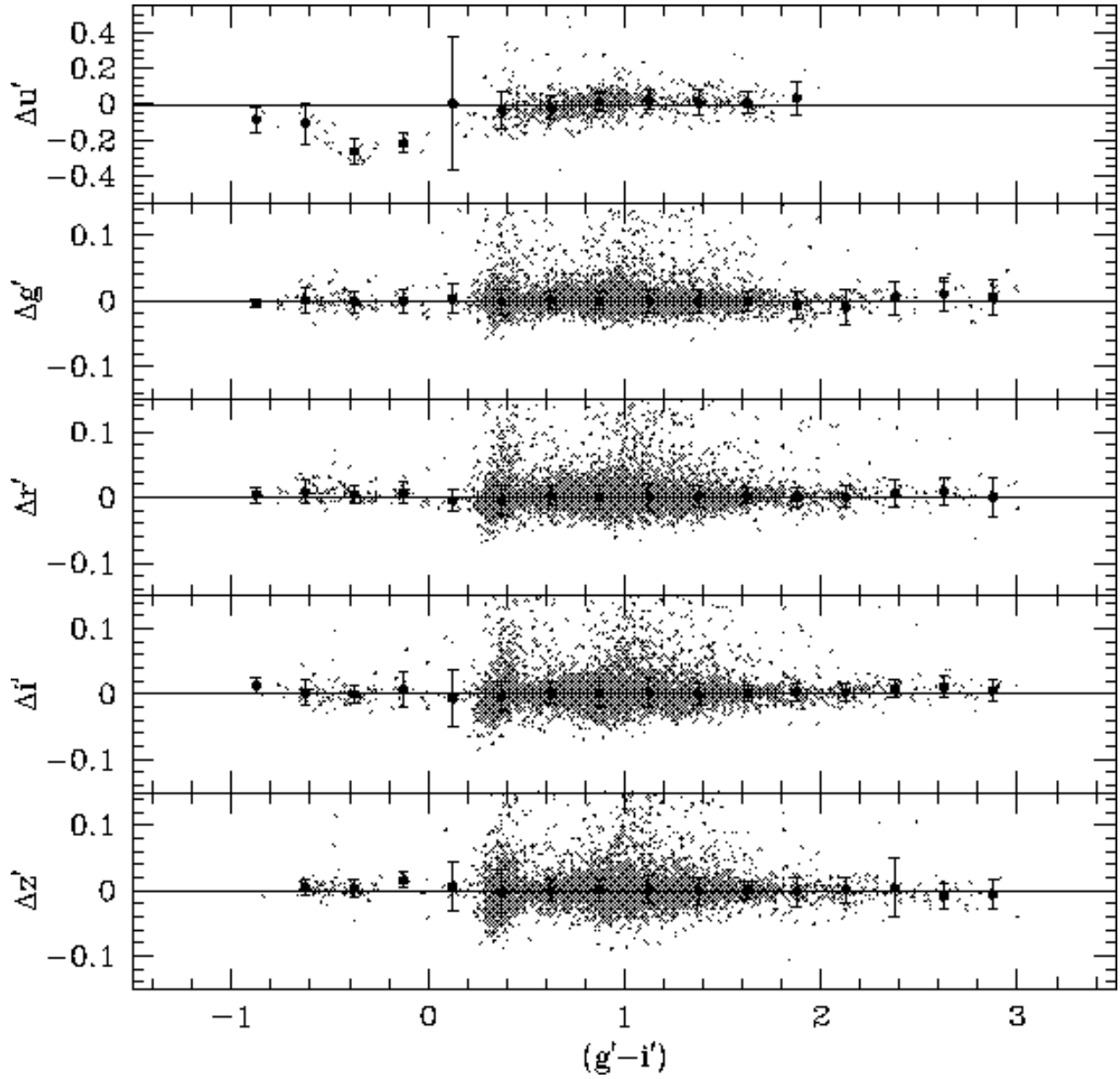


Fig. 4.— Same as Figure 3 except the magnitude residuals are plotted against the standard $(g' - i')$ color. Each large black circle represents the median difference in bins of 0.25 mag in color. Note the strong deviations in $\Delta u'$ as a function of color in the top panel.

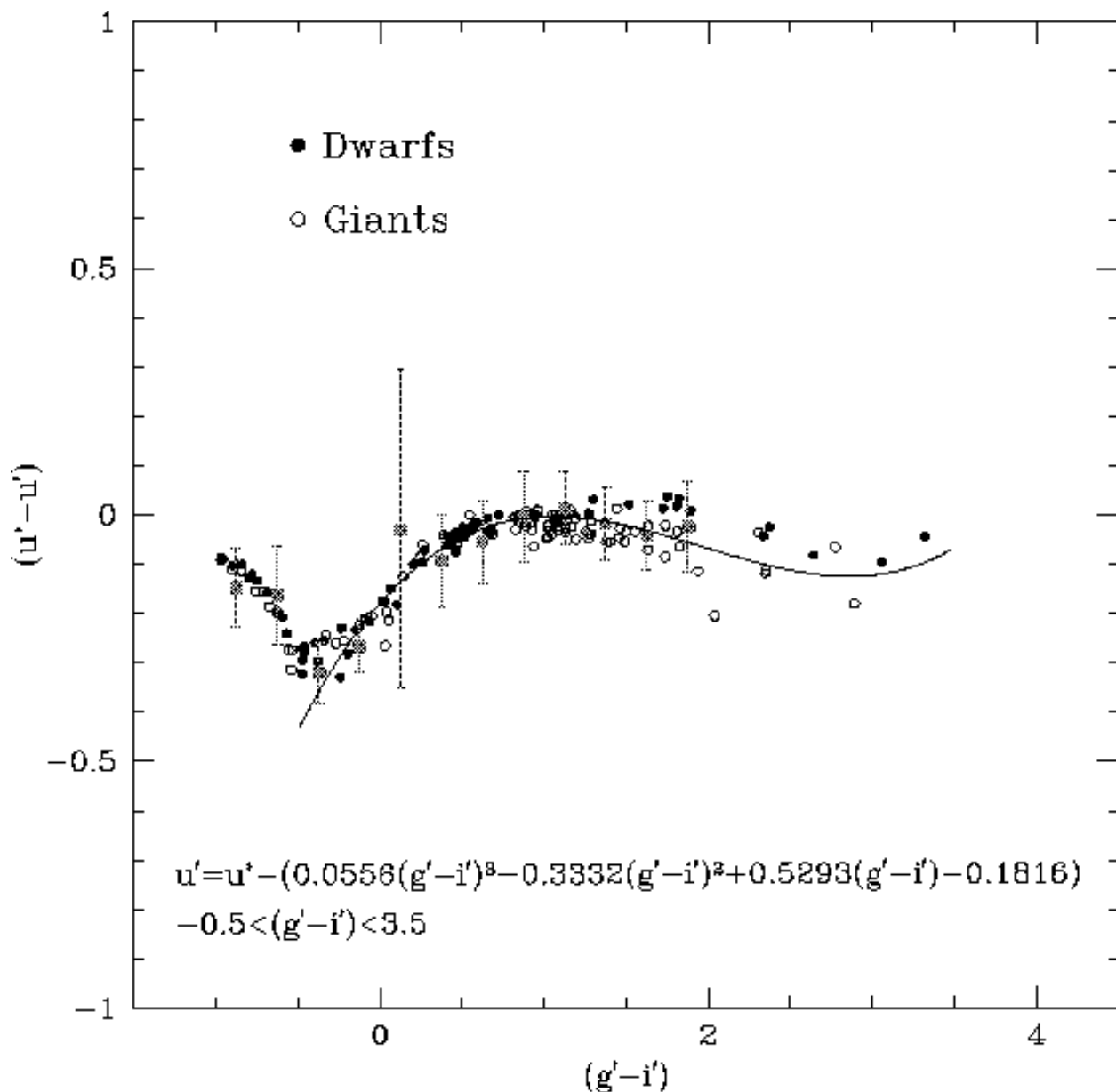


Fig. 5.— Differences between MegaCam’s u^* and standard u' magnitudes as computed by convolving the respective filter transmission functions shown in Figure 2 with the stellar spectral energy distributions as presented by Gunn & Stryker (1983). Giant and dwarf stars in the Gunn & Stryker sample are denoted by open and solid circles, respectively. The median differences in the observed residuals from the top panel of Figure 4 are also plotted as solid gray squares to illustrate the agreement between our own data and the computed magnitudes. The solid line provides the third-order polynomial that was fit to the data to help transform u^* to u' .

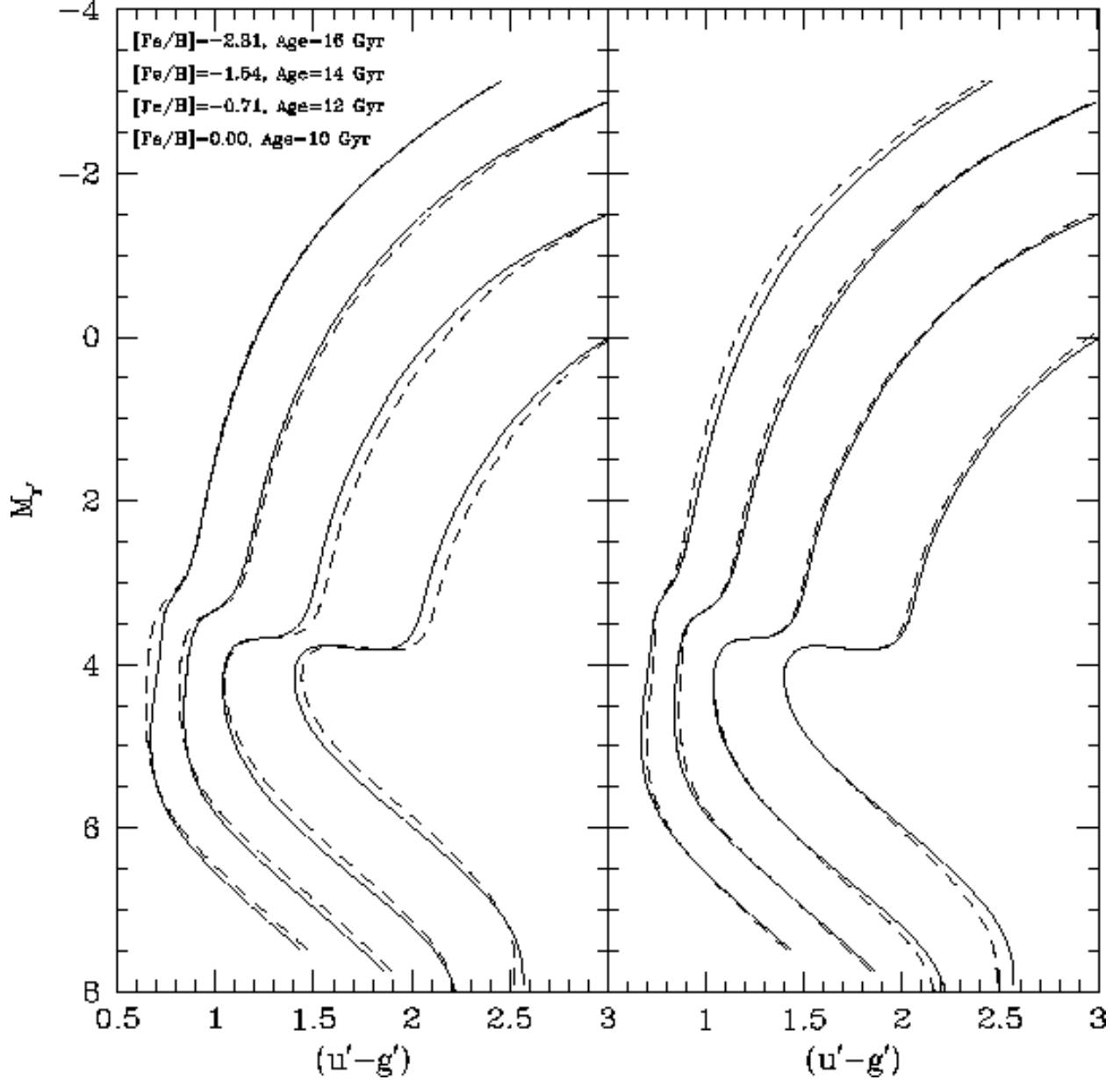


Fig. 6.— Comparisons between theoretical isochrones, with denoted ages and metallicities plotted left-to-right, as transformed to the observed $[(u' - g'), M_r]$ plane using color-temperature relations derived from ATLAS9 synthetic spectra for both MegaCam’s $u^*g'r'i'z'$ (dashed lines) and the standard $u'g'r'i'z'$ (solid lines) filter transmission functions. The left-hand panel compares the two sets of isochrones using the simple linear color term initially derived to transform MegaCam’s u^* photometry to the standard system, while the right-hand panel employs the polynomial transformation denoted in Figure 5. Note the better overall agreement between the two sets when the third-order transformation is used.

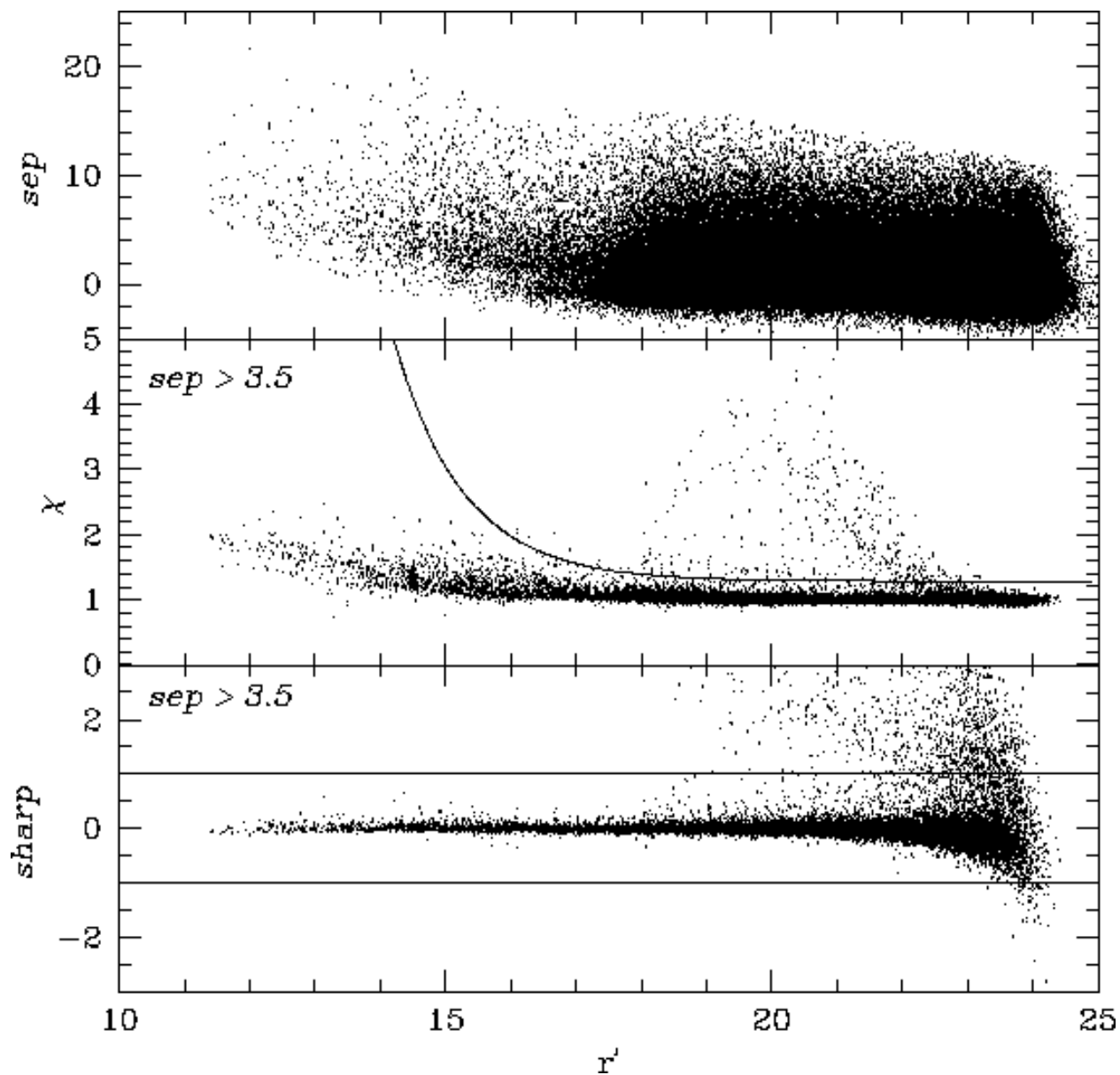


Fig. 7.— Plots of the image-isolation and image-quality indices sep , χ , and $sharp$ versus apparent r' magnitude for stars in the globular cluster M13. Only those stars with $sep > 3.5$ are plotted in the bottom two panels. Stars lying below the solid curve in the middle panel together with those having $-1 < sharp < 1$ in the bottom panel are retained in the sample for the derivation of the cluster fiducial sequences.

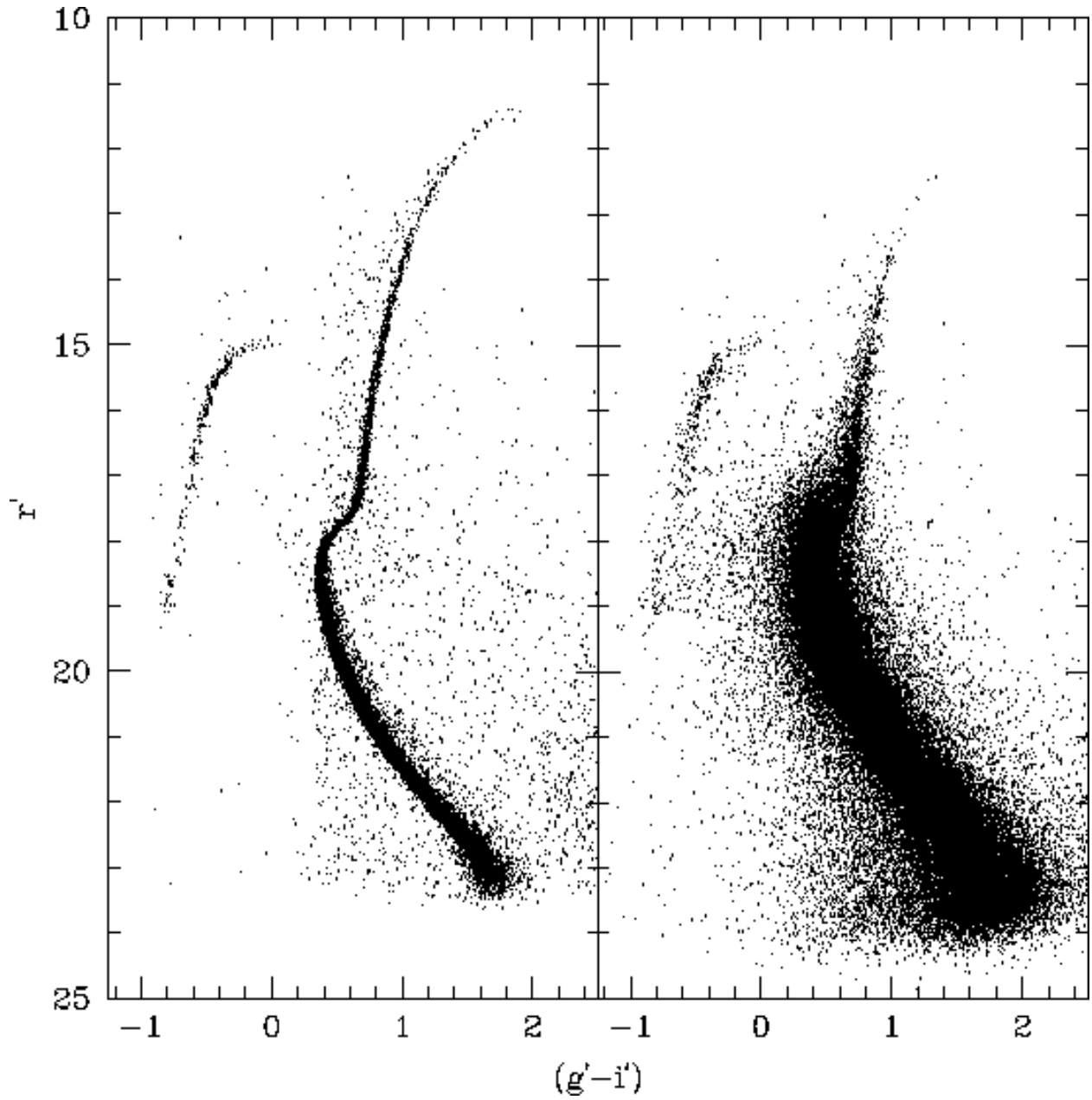


Fig. 8.— Two $(g' - i', r')$ CMDs for stars in the field surrounding the globular cluster M13. The left-hand panel plots those stars judged to have the highest quality photometry on the basis of their *sep*, χ , and *sharp* values as described in the text. The right-hand panel presents stars that are excluded from the deviation of the fiducial sequences due to their poorer photometry. Note the more diffuse nature of the primary cluster sequences in the right-hand panel.

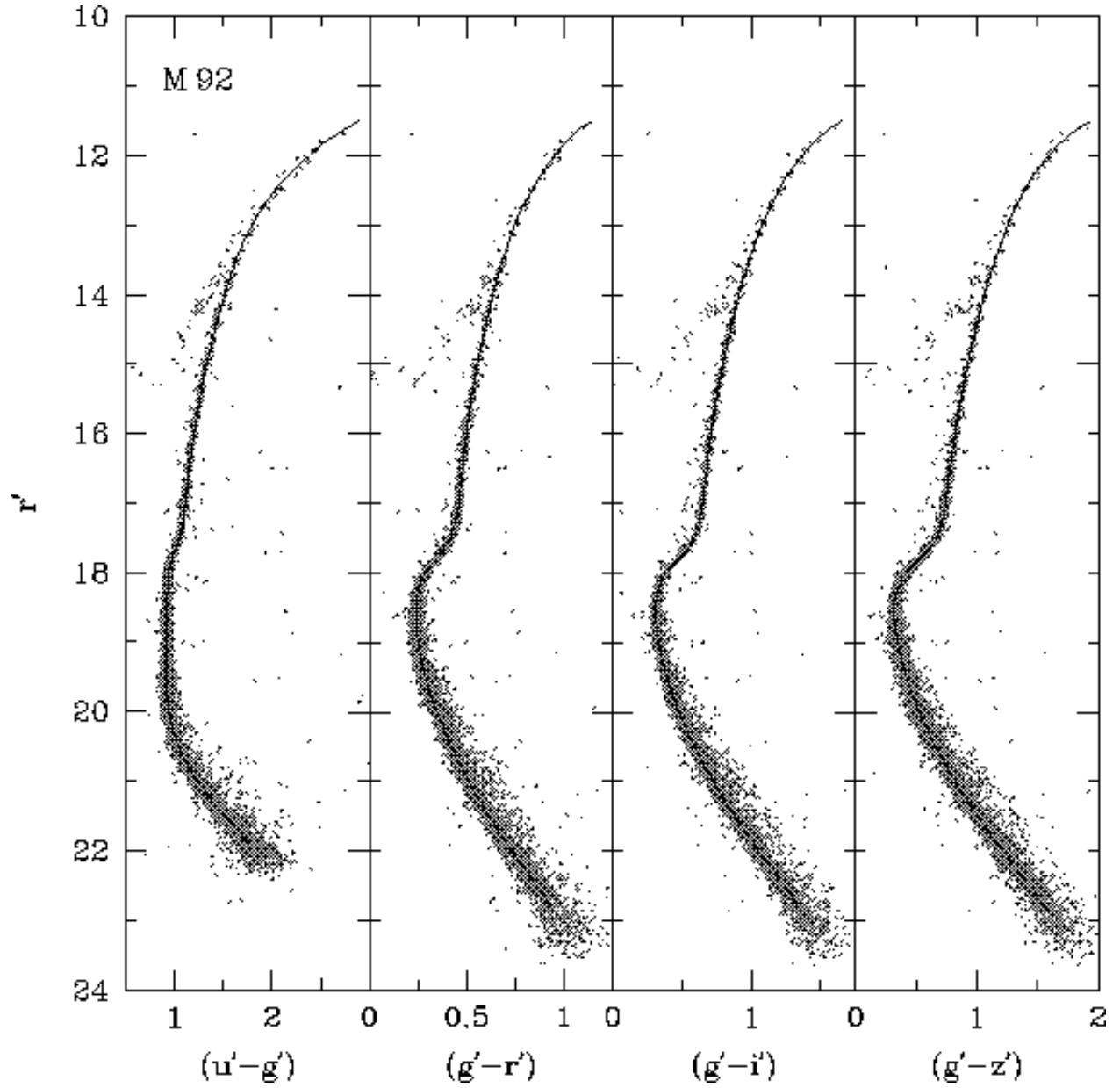


Fig. 9.— Various $u'g'r'i'z'$ CMDs and associated derived fiducial sequences for the globular cluster M92. Each panel includes only those stars judged to have the highest quality photometry based on their values of χ , *sharp*, and *sep*.

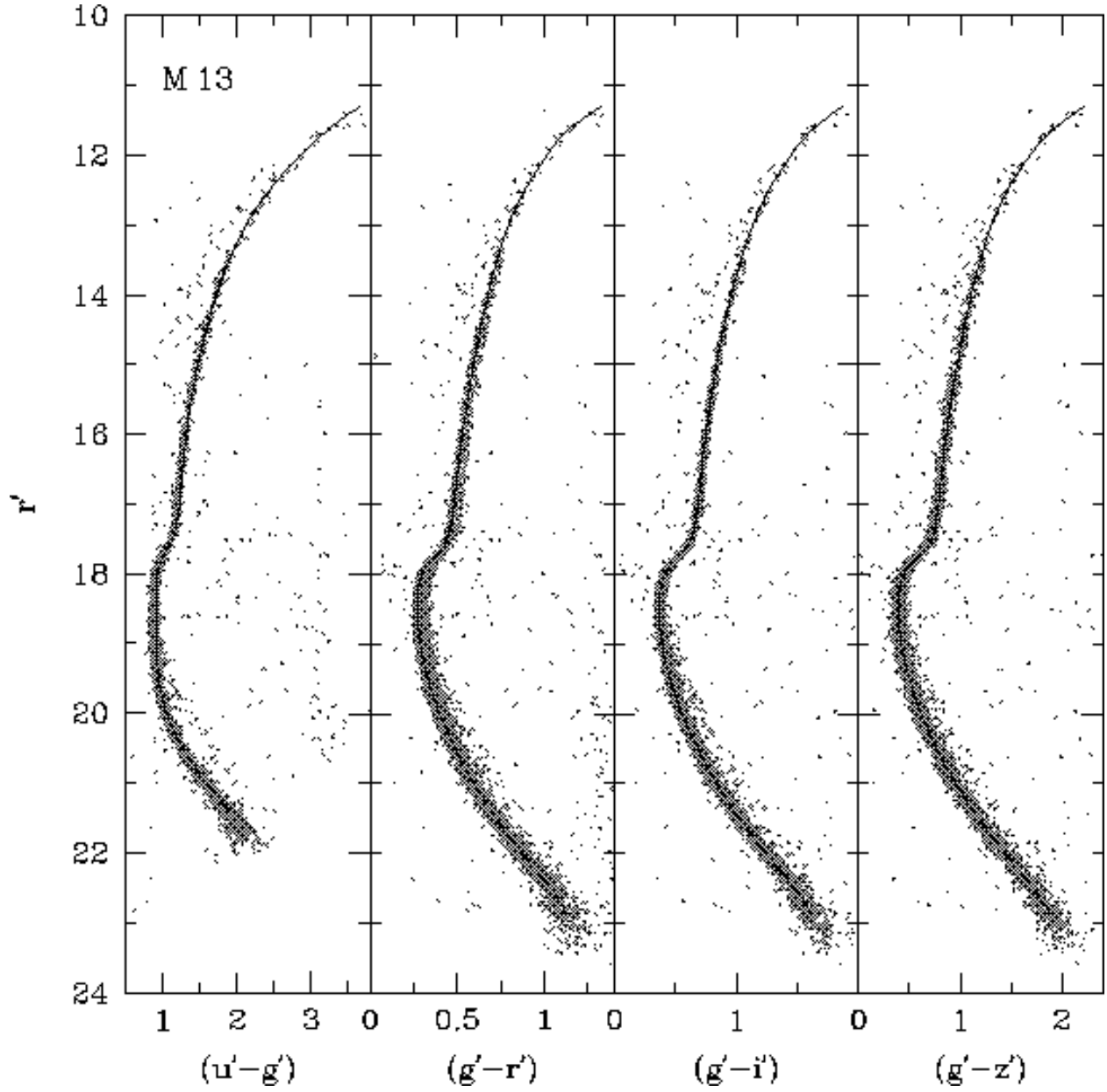


Fig. 10.— Same as Figure 9, but for the globular cluster M13.

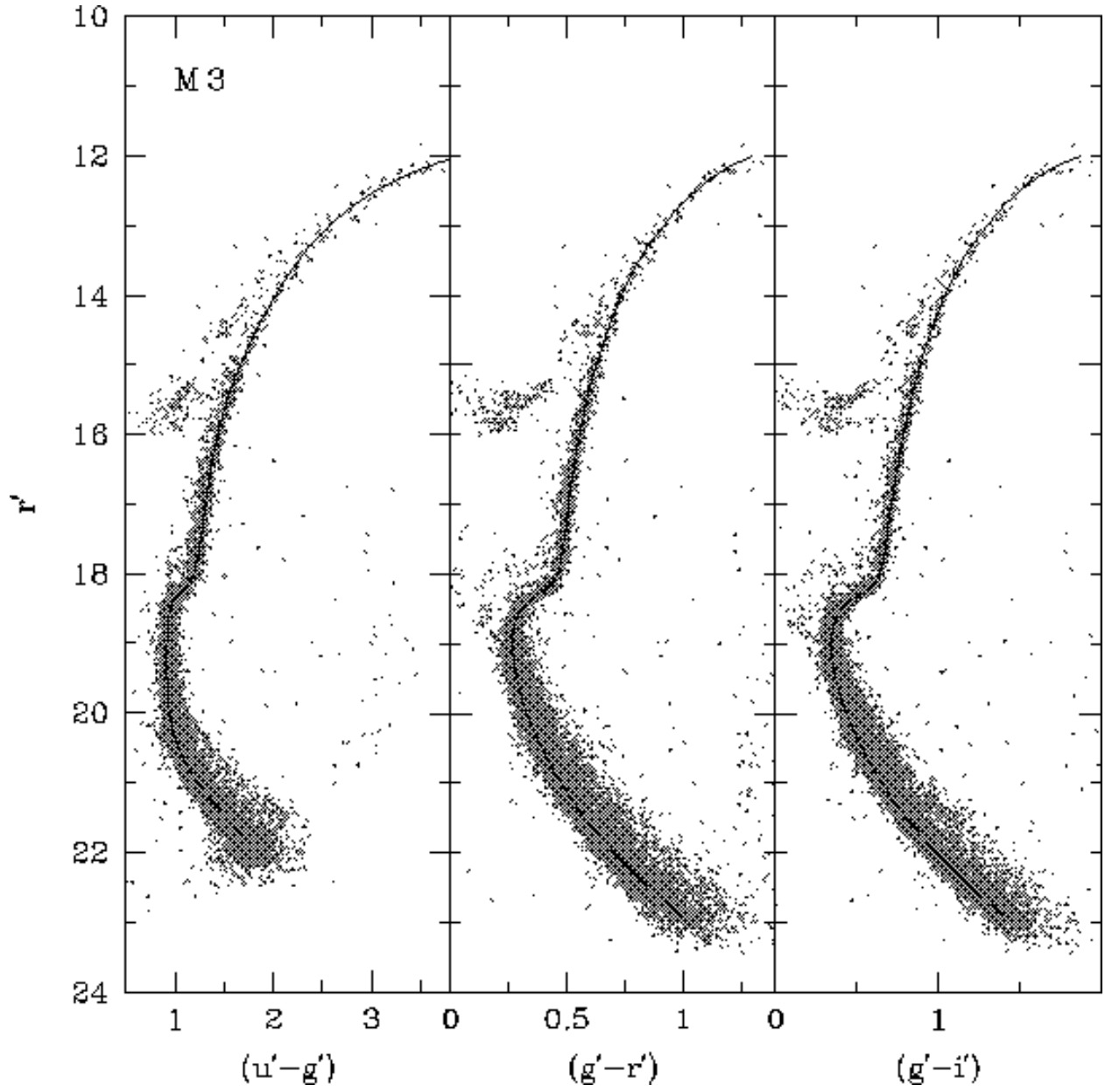


Fig. 11.— Same as Figure 9, but for the globular cluster M3. Note that z' photometry is not available for this cluster.

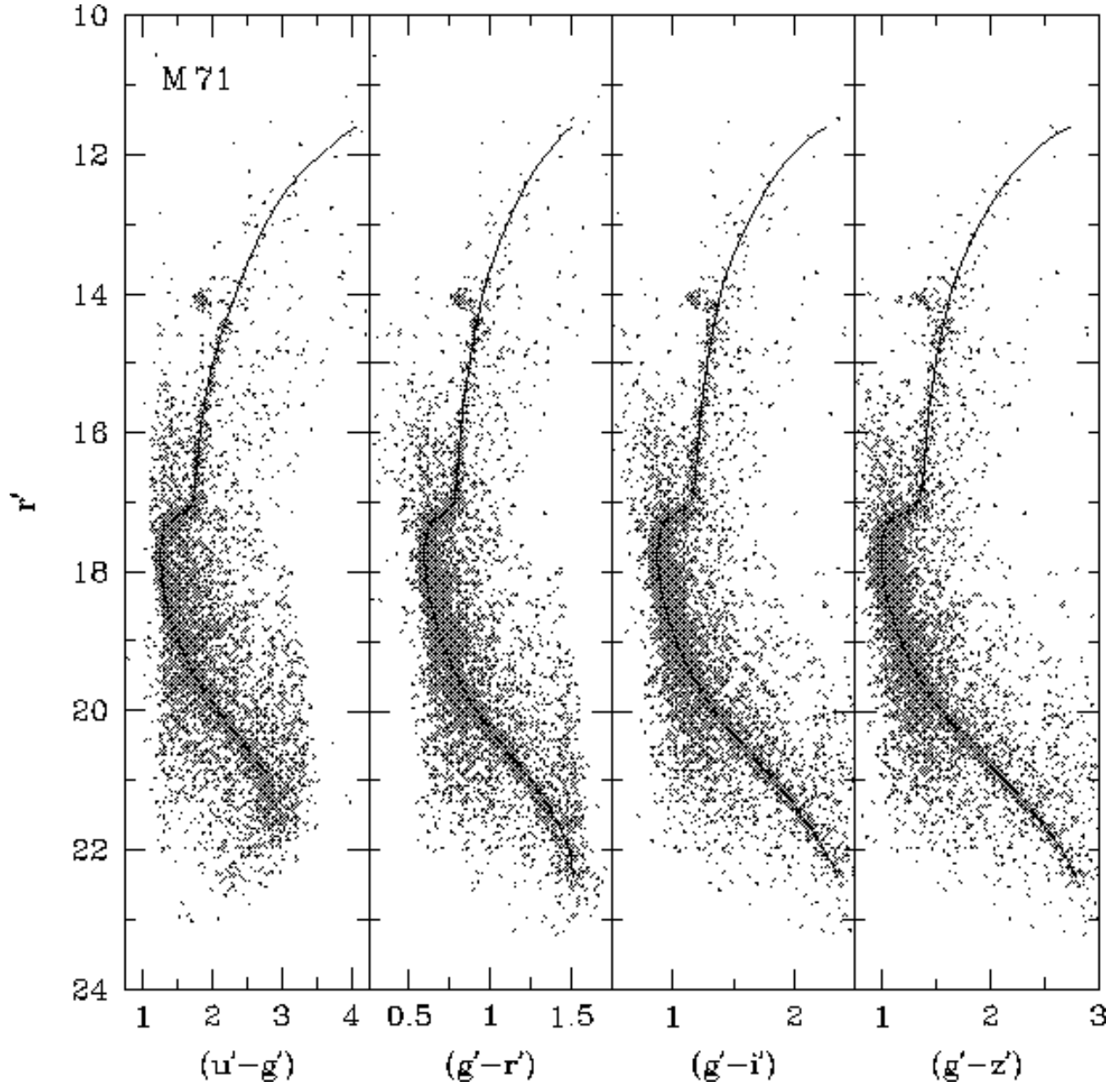


Fig. 12.— Same as Figure 9, but for the globular cluster M71. Each panel plots only those stars that lie within a radius of $2.5'$ from the cluster center in order to reduce field star contamination in the CMDs.

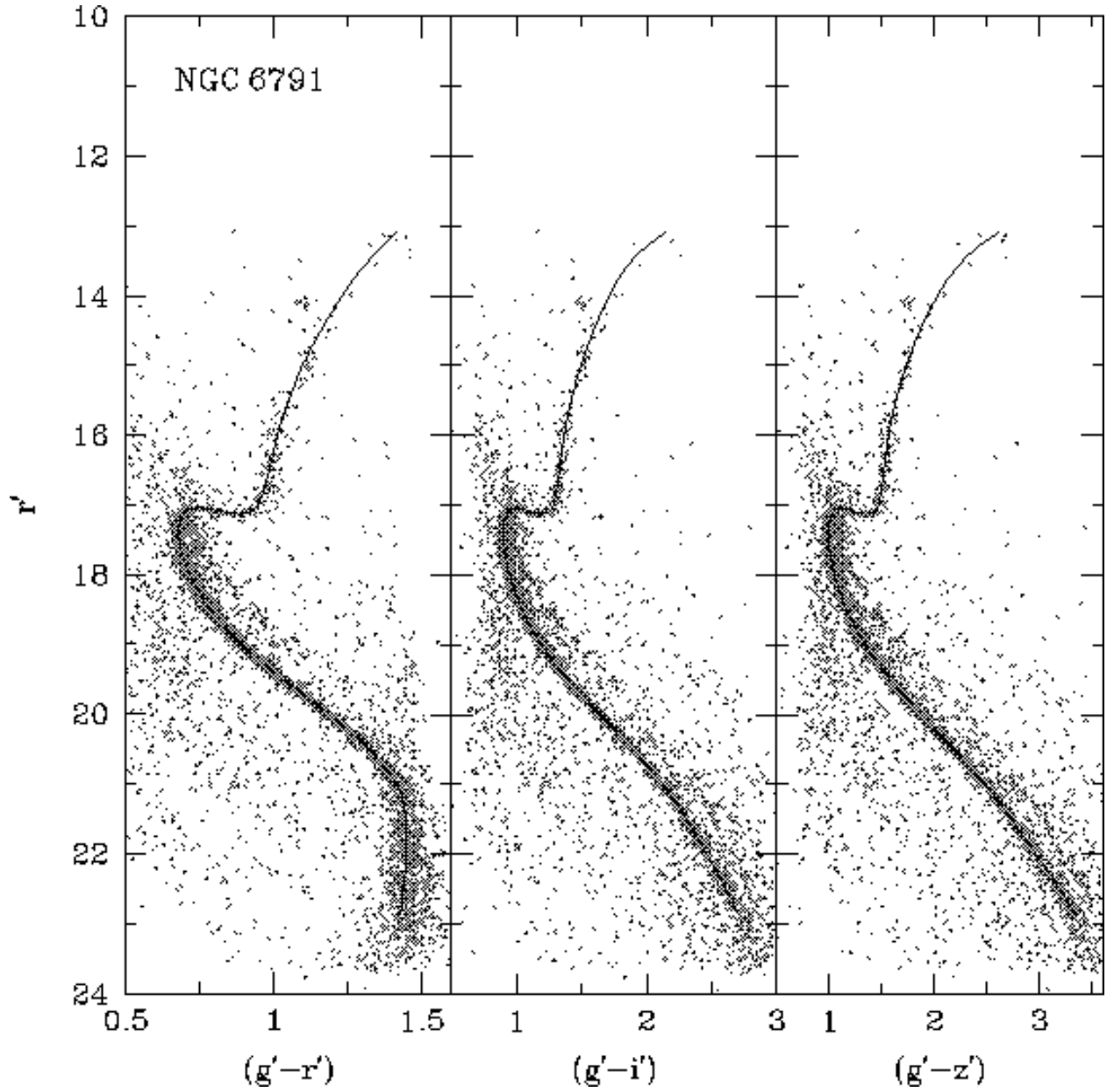


Fig. 13.— Same as Figure 9, but for the open cluster NGC 6791. u' photometry is not available for this cluster. Each panel plots only those stars that lie within a radius of $5'$ from the cluster center in order to reduce field star contamination in the CMDs.